Icing Mitigation by MEMS-Fabricated Surface Dielectric Barrier Discharge

Matthias Lindner [1,*], **Andrei V. Pipa** [2], **Norbert Karpen** [3], **Rüdiger Hink** [2], **Dominik Berndt** [1], **Rüdiger Foest** [2], **Elmar Bonaccurso** [3], **Robert Weichwald** [4], **Alois Friedberger** [3], **Ralf Caspari** [4], **Ronny Brandenburg** [2,5] **and Rupert Schreiner** [1]

[1] OTH Regensburg, Seybothstraße 2, 93053 Regensburg, Germany; dominik.berndt@oth-regensburg.de (D.B.); rupert.schreiner@oth-regensburg.de (R.S.)

[2] Leibniz Institute for Plasma Science and Technology, Felix-Hausdorff-Straße 2, 17489 Greifswald, Germany; pipa@inp-greifswald.de (A.V.P.); ruediger.hink@inp-greifswald.de (R.H.); foest@inp-greifswald.de (R.F.); brandenburg@inp-greifswald.de (R.B.)

[3] Airbus, Willy-Messerschmitt-Straße 1, 85521 Ottobrunn, Germany; norbert.karpen@airbus.com (N.K.); elmar.bonaccurso@airbus.com (E.B.); alois.friedberger@airbus.com (A.F.)

[4] Airbus Defence and Space GmbH, Rechliner Str., 85077 Manching, Germany; robert.weichwald@airbus.com (R.W.); ralf.caspari@airbus.com (R.C.)

[5] Institute of Physics, University of Rostock, Albert-Einstein-Str. 23–24, 18059 Rostock, Germany

[*] Correspondence: matthias.lindner@oth-regensburg.de

Abstract: Avoiding ice accumulation on aerodynamic components is of enormous importance to flight safety. Novel approaches utilizing surface dielectric barrier discharges (SDBDs) are expected to be more efficient and effective than conventional solutions for preventing ice accretion on aerodynamic components. In this work, the realization of SDBDs based on thin-film substrates by means of micro-electro-mechanical-systems (MEMS) technology is presented. The anti-icing performance of the MEMS SDBDs is presented and compared to SDBDs manufactured by printed circuit board (PCB) technology. It was observed that the 35 µm thick electrodes of the PCB SDBDs favor surface icing with an initial accumulation of supercooled water droplets at the electrode impact edges. This effect was not observed for 0.3 µm thick MEMS-fabricated electrodes indicating a clear advantage for MEMS-technology SDBDs for anti-icing applications. Titanium was identified as the most suitable material for MEMS electrodes. In addition, an optimization of the MEMS-SDBDs with respect to the dielectric materials as well as SDBD design is discussed.

Keywords: SDBD; MEMS; anti-icing; low-temperature plasma; aerospace engineering

1. Introduction

Preventing ice buildup on aerodynamic components is of primary importance to flight safety [1,2]. Ice accumulates especially on the front components of an aircraft, severely limiting its performance by increasing drag and decreasing lift. The prevention of ice formation is often referred as an anti-icing and the removal of already present ice as a de-icing. Current investigated technologies such as liquid-based systems [3], pneumatic systems [4,5], thermal systems [6] or electro-thermal systems [7,8] cover a wide range of research areas.

Whereas the related topic of plasma actuators (PA) for flow control applications is widely studied [9–20], there is recently a growing interest in the study of surface dielectric barrier discharges (SDBDs) as an anti-icing and de-icing system [21–30]. Probably Meng et al. [24] and Cai Jinsheng et al. [21] were the first who reported experimental results indicating that SDBDs can work as an anti/de-icing system. They used Kapton foils wrapped around a cylinder with copper tape as electrodes. The ice protection effect is explained by a temperature increase of the surface measured by a thermal imaging camera. Tian et al. [22] used acrylonitrile butadiene styrene (ABS shells) as dielectric for SDBDs and

mounted it on an airfoil. They concluded that the anti-icing with SDBDs is more efficient compared to ohmic heating systems, even accounting that the main power consumption of SDBD also depends on the efficiency of its power supply.

Kolbakir et al. and Meng et al. [23,25] investigated different geometries and concluded that a streamwise layout, where the electrodes are orientated along the flow is better for anti-icing than a spanwise layout (electrodes orthogonal to the flow). They suggest that this effect can be caused by the 70 μm thick copper electrodes, which significantly increases the surface roughness and induce premature turbulences on the wing disturbing the laminar flow, through which the SDBD generated heat is transported away from the surface [25]. Chen et al. [26] compared the SDBD-plasma heating with electric heating in a droplet-evaporation study by applying the same surface temperature. They could show that plasma heating was 6.5 times faster and, in addition, that the plasma seems to evaporate water droplets on the surface by subsequently dividing water drops into smaller and smaller droplets.

Wei et al. [27] proposed a nanosecond pulse operated SDBD (nSDBD) heat knife with a stream-wise electrode configuration. Their nSDBD locally cuts the ice which is then blown away by the passing air flow. The use of such a heat knife is particularly conceivable at the leading edge of an aerodynamic component. Rodriguez et al. [31] investigated the heat generation mechanism of SDBDs in more detail and assumed that materials with a high permittivity generate heat more efficiently, whereas the dissipation factor plays only a minor role. This study shows that the de- and anti-icing effect is influenced by the discharge geometry as well as the materials being used. A full understanding of the impact of such properties is still missing.

The goal of the present work was to examine Micro-Electro-Mechanical Systems (MEMS) technology fabricated actuators for anti/de-icing applications. The ability to manufacture SDBDs with extremely thin and fine structured electrodes is the main advantage of the MEMS-technology. However, the thin electrodes can exhibit strong erosion under the aggressive discharge environment [32]. Minimization of electrode erosion is the main challenge MEMS-technology has to deal with. For this purpose our previous studies on the electrode material [32] were expanded in this work. The degradation of the dielectric material can be avoided by using inorganic substrates [33]. A further challenge of the technology development was the reduction of the discharge operation voltage to ensure a safer operation of the SDBDs by increasing electromagnetic compatibility. This can be achieved by reducing the dielectric thickness [34]. For this reason SDBDs manufactured on 500 μm thick borofloat glass and 150 μm zirconia ceramic substrates were examined.

2. SDBD Preparation

2.1. MEMS Fabrication

MEMS technology enables an implementation of the desired geometry with sub-micrometer accuracy. The MEMS manufacturing steps and principles are shown in Figure 1. In a first step, the substrates were pre-cleaned in an isopropanol and an acetone ultrasonic bath for 10 min. Then the 4-inch substrates were spin coated at 4000 rpm with an AZ 5214 NV image reversal photoresist and soft-baked for 60 s at 100 °C. The electrode pattern was structured by optical lithography (365 nm) and after the reversal image procedure the substrates were developed in AZ 726 MIF to remove soluble photoresist areas. In a fourth step the samples were metallized by an electron beam physical vapor deposition (EB-PVD), with which the electrode thickness can be adjusted accurately to a few nanometers. A lift-off process in acetone removes the AZ 5214NV and finalizes the fabrication process of one electrode side. The counter electrode was produced analogously after turning the sample over. Alignment marks on the sample ensure a precise counter-electrode positioning.

An erosion study was conducted to evaluate an appropriate electrode material. For this purpose, three SDBDs were prepared on a borofloat glass substrate for each electrode material to be investigated. The SDBDs were then operated slightly above the ignition voltage for 30 and 60 min, respectively. Scanning electron microscope (SEM) images of

the non-operated and the two eroded samples are presented in Figure 2. The high-voltage electrode of the SDBD is colored in false-color in each picture. The images were taken with a JEOL JSM-6510 at an inclination angle of 60° after sputtering a few nanometers of gold onto the samples to avoid insulator charging effects and, thus, to improve the image quality. Note that the supplementary provides the original SEM photos at a higher resolution (Supplementary S1–S5).
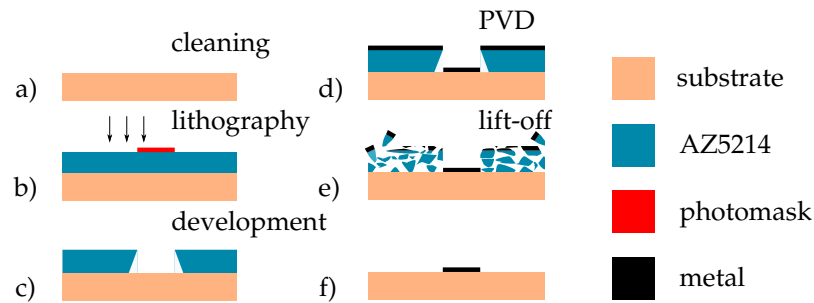

Figure 1. Principles and technological steps of the MEMS-manufacturing process.
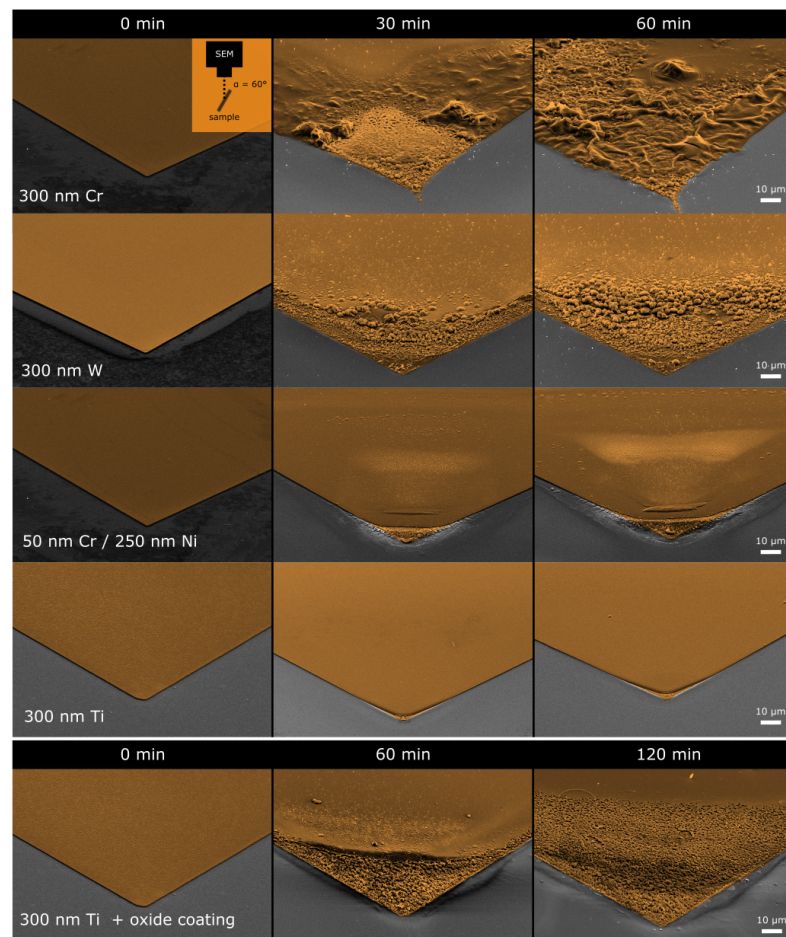
Figure 2. Erosion study to find a suitable material for the SDBD electrodes. The SEM images of the MEMS-fabricated SDBD electrodes taking at an inclination angle of $\alpha = 60°$ and displayed in false color. The left column presents the electrodes directly after the fabrication with indication of their materials or material combinations. The other columns shows the electrodes after SDBD operation by a $V_{rms} = 2.2\,\text{kV}$ sine wave with a frequency of $f = 1\,\text{kHz}$ during the time displayed in the column's index.

A chromium (Cr) layer provides an excellent adhesion to the glass surface, however, it erodes quickly under air plasma operation, as it is shown in Figure 2. Using Cr as adhesion promoter a second metal layer can be used to protect the electrodes from a fast erosion.

Since the erosion of MEMS-fabricated SDBDs [35,36] is of extraordinary importance for the durability of the device, erosion studies can already be found in the literature [16,32,33,37]. It was shown that tungsten (W) [16,33,37] has a good resistance against the destructive forces of the low-temperature plasma. In [32], we reported on the erosion of the commonly used Cr/Cu electrodes and also showed that a protective layer of gold (Au) restricts the erosion only to a certain degree. In the same study Cr/Ni electrodes [32] were found to be the most suitable electrode metals in terms of erosion. The present study now compares the Cr/Ni electrode erosion to the tungsten electrode erosion. Figure 2 exhibits that Cr/Ni depicts a better erosion resistance than tungsten, however, the additionally analyzed titanium (Ti) electrodes revealed the least signs of erosion.

Note that titanium was already used by Pescici et al. [16], but only as a 10 nm thick adhesion promoter in a multi-layer high-voltage electrode composed mainly of tungsten. They also propose a TiN layer coating since it is a well-known wear resistant, however, it was not evaluated whether this protective layer really diminishes the erosion. Our study indicates that a EB-PVD deposited 100 nm Al_2O_3-oxide layer has no protective effect, see Figure 2.

Finally, two dielectric substrates were processed in an EN ISO 14644 standard clean-room at the OTH Regensburg. Both dielectrics are of inorganic origin to mitigate the dielectric degeneration by the plasma [38]. Borofloat 33 glass from Schott and 3YSZ-Sensor from Kerafol, which is a special partly stabilized zirconia ceramic with 3 mol% Yttria. The zirconia wafers were metallized by a 200 nm Ti layer, whereas the glass wafers were metallized by Cr/Ni with a final thickness of 260 nm because the results of the Titanium erosion were not known in the moment of the fabrication. With the later application in mind, a 150 μm thick zirconia substrate was used, which is still flexible despite its inorganic origin and, thus, can be adapted to any shape using lightweight construction technology as it has already been shown in [32].

2.2. Geometry and Sample Preparation

The common strategy of investigation is to include a reference area on the sample in addition to the SDBD due to the stochastic nature of the icing process. For this reason, only the lower half of the sample (24.5 mm × 66.5 mm) is equipped with the anti-icing SDBDs and the upper half serves as a reference area. A sketch of the electrode geometry G1 is depicted by Figure 3. The SDBD consists of 16 high-voltage electrodes and a single continuous ground electrode on the other side of the substrate.

The high-voltage electrode was micro-structured by right-angled triangles with a base of 250 μm as shown in the inset of geometry G1 in Figure 3. The same triangle structure was also used in the erosion studies of Figure 2. The micro-structure was intended to increase the electric field locally which can be an advantage at combining SDBDs with biomimetic structures [39]. In our case, the structure has a minor influence on the ignition voltage.

The same geometry was realized with the PCB as well as with the MEMS-fabrication to compare the performance of differently manufactured discharge arrangements in the experiment. The PCB-samples were manufactured on the substrate FR-4 TG135 by IBR Leiterplatten GmbH & Co KG. In the PCB-based fabrication, glass fibers woven in epoxy resin (FR-4) are pressed together with thin copper foils which severely restricts the smallest possible thickness of the copper layer. The post-processing (etching, micro-milling) of these relatively thick (35 μm) foils then leads to a rounding of the desired electrode geometry. The difference between PCB and MEMS electrodes is clearly depicted in the SEM images of Figure 4. Note that the size of the observed samples restricts the inclination angle to 55° for technical reasons that makes the width of the MEMS electrodes less noticeable.
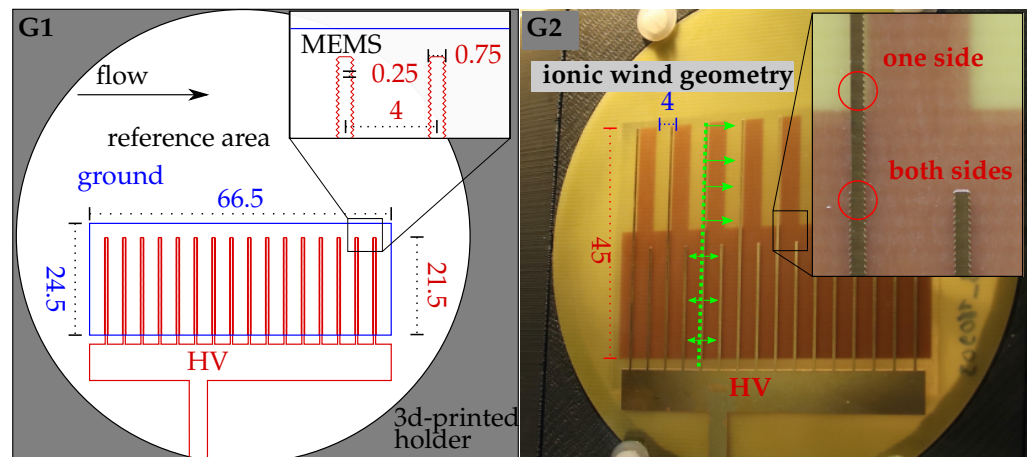
Figure 3. Sketch of the SDBD geometry G1 (**left**) and a photograph of the SDBD manufactured with geometry G2 (**right**). The high-voltage (HV) electrodes are at the substrate top (red) and the ground electrode on the backside (blue) of the substrate. All dimensions are shown in millimeters. The green arrows on the photograph indicate the direction of the ionic wind generated by one electrode.
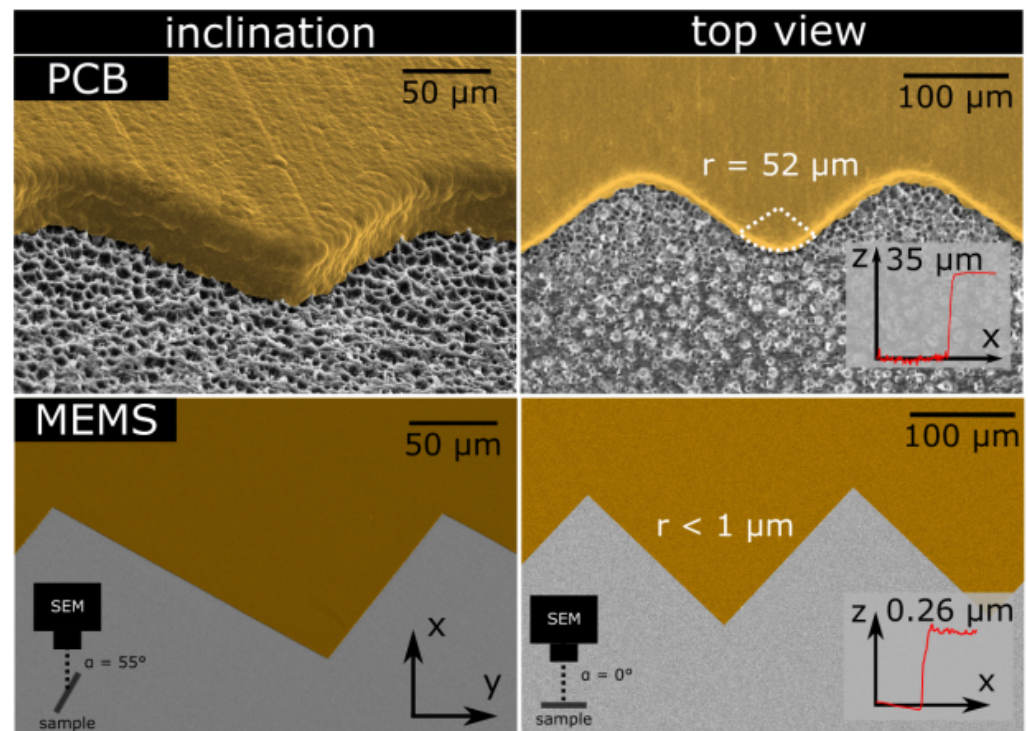

Figure 4. SEM images of the PCB-fabricated electrodes (**top**) compared to MEMS-realized electrodes (**bottom**). The pictures were taken with an inclination angle of $\alpha = 55°$ (**left**) and from top view (**right**). The two insets show profilometer measurements of the electrode steps.

On the basis of our previous research [32,34] a second electrode pattern G2 (right side of Figure 3) was implemented to investigate the impact of the ionic wind. The green arrows in Figure 3 indicate the generated ionic wind direction. The actuator area creates an ionic wind in downstream direction. At the SDBD area the ionic wind is generated in both directions neutralizing itself. A detailed description of the generation mechanism and the implications of the ionic wind can be found in Kriegseis et al. [15] and the references therein. For the sake of simplicity and fast prototyping, this geometry was realized only on PCB samples.

Additional investigations were carried out to characterize the dielectric materials. For data concerning the substrate roughness, the surface wettability, the dielectric permittivity

and the dielectric dissipation factor, we refer to the substrate properties column of Table 1. See Supplementary S6 and S7 for more information.

Table 1. Overview of the measured materials, the measured surface roughness (σ), the dielectric constant (ϵ_r), the contact angle (Θ), the loss tangent (δ), the used substrate/dielectric thicknesses (d_{diel}), the manufacturing processes (method), the electrode thickness (d_{el}) and the electrode material. The table also shows the icing wind tunnel parameters at which the experiments were conducted, namely the operation Voltage (V_{rms}) of the SDBD and its measured power scaled to the electrode length (P/L), the applied air speed (v) and the temperature (T). * estimated from measurements at ambient air.

	Substrate Properties					Electrodes			iCORE			
Name	σ [µm]	ϵ_r	Θ	tan δ	d_{diel} [µm]	Method	d_{el} [µm]	Metal	V_{rms} [kV]	P/L [W/ m]	v [m/ s]	T [°C]
FR-4	0.70	5.5	106°	0.008	500	PCB	35	Cu/Au	5.4	7.2 ± 0.5	50	−17
Borofloat glass	0.02	4.3	99°	0.011	500	MEMS	0.26	Cr/Ni	5.4	7.2 ± 0.5	27	−18
Zirconia ceramic	0.15	28.3	68°	0.015	150	MEMS	0.2	Ti	2.0	~ 20 *	30	−20

3. Electrical Characterization

3.1. Setup

A Chroma (Model 61603) wave function generator and a high-voltage custom-built transformer (Bremer Transformatoren GmbH) provided the sinusoidal high-voltage with a frequency f of 1 kHz for the SDBDs, see Figure 5. The high-voltage was measured using a Tektronix P6015A 1:1000 high-voltage probe. WIMA FKP1 capacitors were utilized to measure the charge transferred in the SDBDs. The exact value of the measurement capacitance was determined with a GW Instek (Model LCR- 817) LCR-meter at the measurement frequency 1 kHz. For the glass and the FR-4 samples a 32.74 nF measurement capacitor was used and due to a larger capacitance of the zirconia SDBD a 151.45 nF measurement capacitor was used there. The voltage drop across the capacitor was measured by a dual wire and connected via BNC to the Rohde & Schwarz RTO2034 oscilloscope, which averaged the charge-voltage plot of the samples over 200 high-voltage cycles. The charge-voltage characteristics were integrated by a python3 script to obtain the dissipated power of the SDBDs. For further details on the technique of power measurements see [40,41] and references therein.
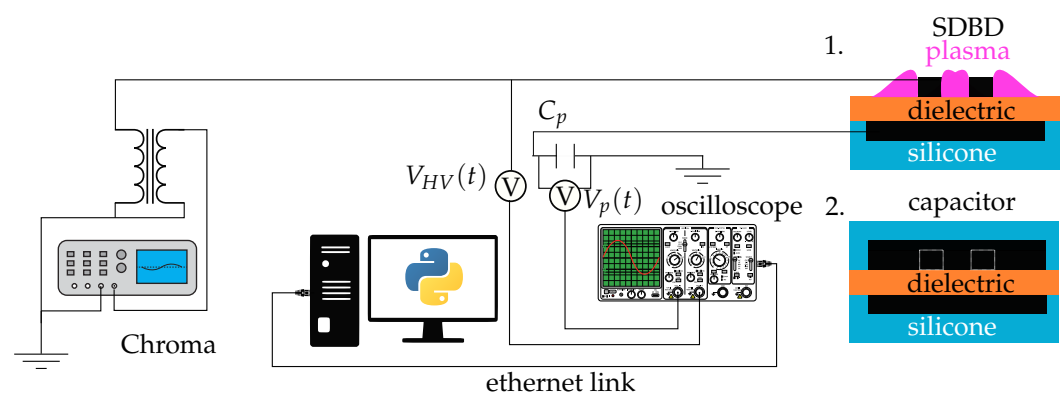

Figure 5. Measurement setup for the plasma power and the estimation of the dielectric losses. Configuration 1 is a sketch of the SDBD sample. Configuration 2 represents the capacitor setup.

Additional experiments were carried out to estimate the power loss in the dielectric. For this purpose, the high-voltage electrodes were covered by a conductive copper tape above the area of the ground electrode and were then embedded in flowable silicone (Dow Corning 3140 RTV). This additional insulation suppresses the plasma formation at all electrodes. In the following these samples are further called "capacitor samples" and are sketched as configuration 2 in Figure 5. Both configurations were operated at ambient air and room temperature.

3.2. SDBD Power

The glass and FR-4 samples have the same thickness (500 µm), a similar permittivity, see Table 1, and for both the discharge is ignited around $1.4\,kV_{rms}$. Photos of the glass SDBD at different applied voltages, shown by Figure 6, demonstrate the expansion of the discharge area. The discharge started at electrode tips with a low luminosity. The luminosity of the spots increases with the voltage and the discharge expands around the electrode edges. The luminosity of the discharge is decreasing with the distance from the electrodes as it is typical for SDBDs (see, e.g., Hink et. al [34]). The discharges occupy the whole area above the ground electrode at $2.8\,kV_{rms}$. After that, a further increase of the voltage amplitude increases the luminosity of the discharge, however, the discharge area stays the same. More detailed photographs of the discharge can be found in Supplementary S8.
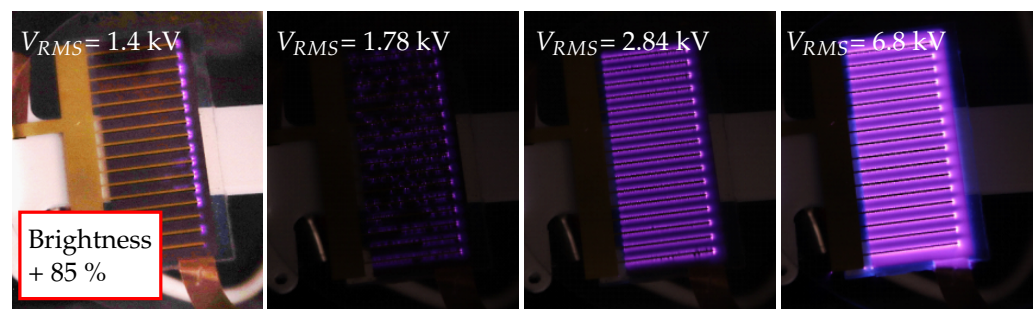

Figure 6. SLR-camera images of the plasma expansion of the glass SDBD at different operating voltages.

The ignition of the discharges for the 150 µm thick zirconia SDBD occurs slightly above $0.7\,kV_{rms}$, with filaments randomly [42] distributed over the length of the high-voltage electrode, see Supplementary S9. The results of the power measurements are shown in Figures 7 and 8. The up and down cycle of the voltage-sweep were performed to visualize a possible degradation of the samples due to the erosion of either the electrodes or the dielectric. The power was scaled to the effective length of the high-voltage electrodes (L = 0.696 m) which was measured disregarding the microstructure as introduced by Hink et al. [34]. The power of a freely expanding SDBD increases with a cubic behavior of the applied voltage ($P \sim V^3$), see [43]. Considering Figure 6 the discharge expansion of the glass SDBD is limited by the dimensions of the ground electrode and as well as the neighboring high-voltage electrodes. Furthermore, starting from $2.8\,kV_{rms}$ the power increases just linear with the applied voltage, similar to the volume dielectric barrier discharges [41]. A similar power voltage dependence is also obtained for the FR-4 sample and the measured values agree for both materials within the experimental errors. The dissipated power at the zirconia sample has a stronger dependency on the voltage due to the extremely thin dielectric with a higher dielectric constant [34,40].

The power measurements in the capacitance configuration were straight forward for FR-4 and glass sample. The up- and down-cycle measurement were similar within the scope of the measurement accuracy. Both substrates have similar dielectric properties, see Table 1, and the power losses in the dielectric do not exceed 20%.
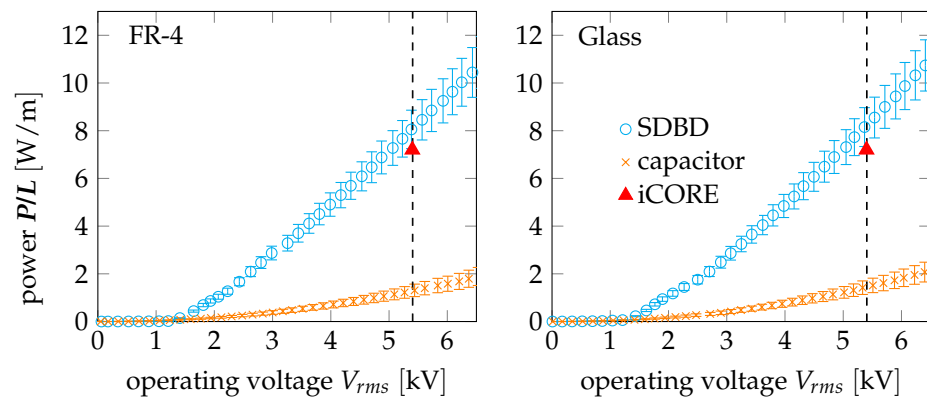
Figure 7. The consumed power for the glass and the FR-4 SDBDs measured for different operation voltages at both configurations of Figure 5. The dashed line represents the operation voltage used in the later icing experiments. The red triangles are the power values measured directly during the icing experiment.
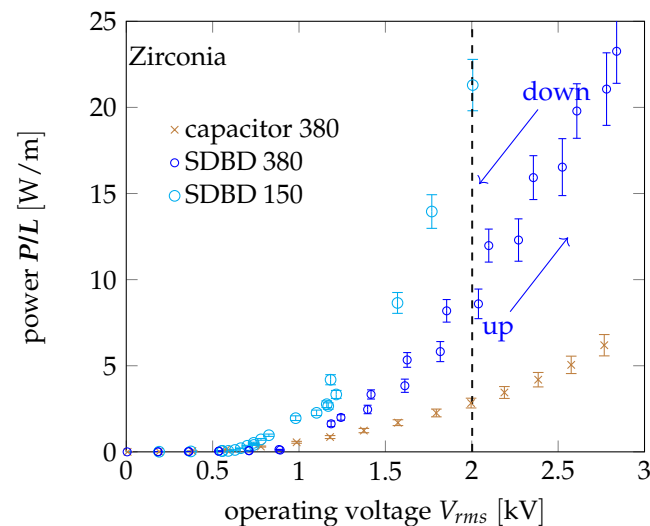

Figure 8. The measured voltage-power relation for the zirconia SDBDs with the 150 μm and 380 μm thick substrate. A thicker (380 μm) substrate was used to estimate the power losses dissipated in the zirconia. Due to the heat-sensitive zirconia substrate different power values were measured during the up- and down-cycle.

In the case for the 150 μm zirconia sample, surprisingly, an electrical breakdown of the dielectric occurs at the capacitor configuration at voltages below $1\,\text{kV}_{\text{rms}}$. Presumably, due to the dielectric losses the substrate temperature increases and also the flowable silicone around the electrodes restricts the heat transfer to the environment which further heats the substrate. We assume that if a zirconia SDBD is operated for a longer period of time without external cooling, the following mechanism takes action. Dissipated power heats the dielectric. The electrical conductivity of the investigated dielectrics increases exponentially with the temperature [44–46]. Since the applied voltage is constant, the conductivity increase leads to an increase of the current and the dissipated power (P = UI), which again results in a growth of the temperature of the dielectric. The conductivity for zirconia [44] is about 3 orders of magnitudes higher than for glass [45]. At a reasonable local dielectric temperature of 350 °C zirconia already exhibits a conductivity comparable to drinking water. Therefore, at higher temperatures the conductance of zirconia is short-cutting the electrodes and destroying the SDBD. The higher power values for the down-cycle, see Figure 8, can be explained by additional dielectric losses caused by the heat of the zirconia SDBD during the discharge operation. A 380 μm thick zirconia SDBD was used for the

estimation of the dielectric losses to overcome this problem. At $2\,kV_{rms}$ the dielectric losses were estimated to be $\sim$30%, see Figure 8.

4. Icing Experiment

4.1. Setup

The icing measurements were performed at the Icing and Contamination Research facility (iCORE), a laboratory at Airbus Central Research & Technology in Munich [47]. Figure 9 shows the closed-circuit icing wind tunnel with walls consisting of three layers of spruce wood and isolation material. A radial fan accelerates the ambient air to a maximum achievable Mach number of 0.45. Through a heat exchanger cooling system the air can be cooled down to a temperature of T_{min} = $-40\,°C$. The icing cloud can be set with three individual atomization nozzles to liquid water contents (LWC) between $0.1\,g\,m^{-3}$ to $1\,g\,m^{-3}$ at a median volumetric diameter (MVD) of around $20\,\mu m$ per droplet. A Blackfly GigE machine vision camera (frame rate = 30 fps) and a normal single lens reflex (SLR) camera (Canon EOS 5D) were used for recording the experiments.
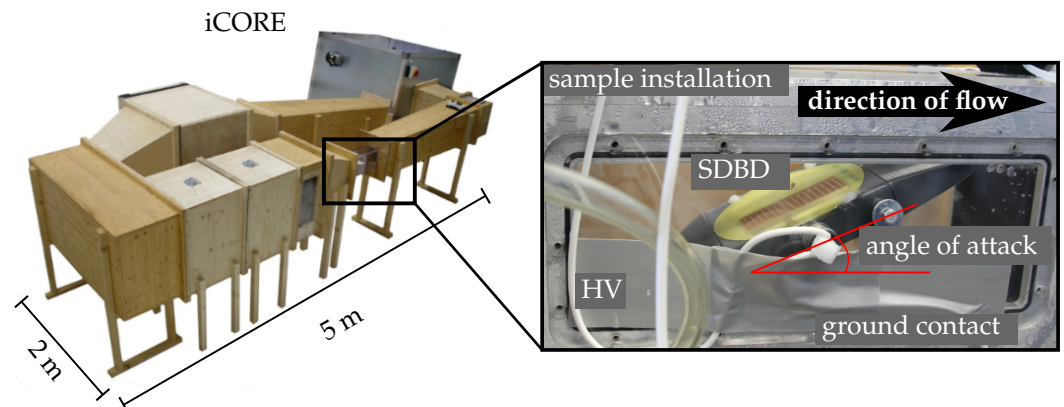

Figure 9. The iCORE, the used icing and contamination research test facility. The left side depicts the whole setup with the air acceleration and cooling system. The right shows an image of the test section with a SDBD sample mounted to an airfoil.

In the experiments the airfoils with the implemented SDBDs were installed with an angle of attack of $\alpha = 30°$ against the direction of the flow, as it can be seen on the right side of Figure 9. This inclination allowed to expose the top surface with the active SDBD to the icing cloud. The electrical contacting of the SDBDs was carried out with a feed-through on the rotary axis. Styrofoam was used as a spacer to keep the high-voltage and the ground wire at a certain distance. The iCORE was started and a wind speed of $v = 50\,m\,s^{-1}$ was applied for the FR-4 measurements. The intention was to operate all experiments at the same iCORE parameters. Due to an increased aerodynamic load during the acceleration of the flow, cracks appeared in the MEMS-fabricated glass substrate. As a preventive action the wind speed was lowered for the MEMS-samples to $v \approx 30\,m\,s^{-1}$. Nevertheless, one of the cracks continued to develop and limited the time of the experiment to the moment when the crack finally resulted in an electric shortcut. The zirconia SDBDs were additionally embedded in glass fiber reinforced plastic (GFRP) as described in [32] for stabilization. After the initialization of the cooling system, a temperature of $T = -20\,°C$ was set. Subsequently, the water spray was started and raised to a rate of $1\,mL\,min^{-1}$ for each nozzle with 3 nozzles in total. Demineralized water was used to inhibit a nucleation of the droplets during free flight through the cold air. The supercooled droplets thus nucleate and freeze only upon impact on a surface, which represents the real aircraft icing process.

4.2. Anti-Icing Results

Images of the SDBDs after the operation in the iCORE with the parameters given by Table 1 are shown in Figure 10. The intention was to operate all samples with a comparable

power consumption. Since the power measurement was not available in the icing wind tunnel for the zirconia SDBD, the power consumption was estimated from subjective perception of discharge intensity.
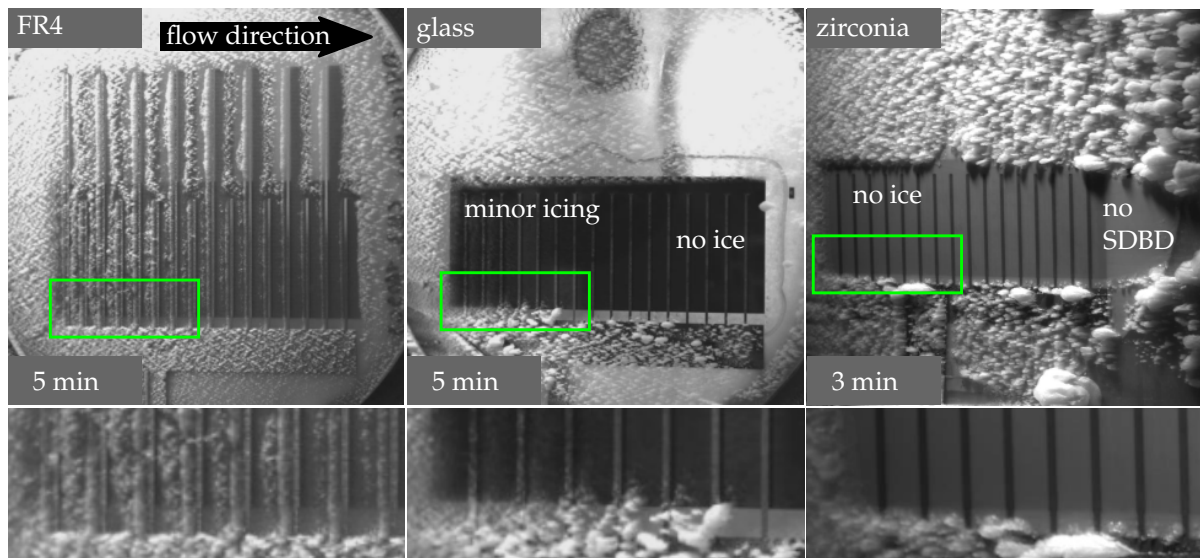

Figure 10. Images of the anti-icing experiment with the three studied materials taken with the machine vision camera from a top view during the anti-icing experiment at the times displayed in the individual lower left corners. The images below depict a magnification of the area marked in green.

Therefore, the zirconia SDBD was operated at significantly lower voltages ($2\,kV_{rms}$) in comparison to the glass and the FR-4 samples ($5.4\,kV_{rms}$). Nevertheless, this low operation voltage corresponds to a power consumption of $21\,W\,m^{-1}$ which is about three times as high as the operation power of the 500 µm thick SDBDs ($7.5\,W\,m^{-1}$ at $5.4\,kV_{rms}$).

The voltage is indicated in Figures 7 and 8 by dashed vertical lines. See also the red triangles for the power values measured during the iCORE experiment. The obtained values are slightly lower compared to the measurements at ambient air. This small difference can be attributed to the higher humidity of the saturated air in the iCORE according to [34,48], however, it is still in the uncertainty range of the electrical measurements.

At the given test condition, which is referred to as rime ice condition, supercooled droplets in the air flow impact on the sample surface and freeze instantly. This mechanism leads to the steady growth of an ice column against the wind direction [21,49]. The likelihood of a supercooled water droplet adhering to the surface, and thus the severity of ice formation, depends on environmental conditions, surface wettability, and surface roughness [50,51]. Due to the hydrophilic properties of the zirconia ceramic, ice formed more rapidly on the reference area, so the duration of the experiment was shortened to 3 min. The growth of the ice column is seen much more pronounced on the zirconia surface then on the glass or the FR-4 after 5 min of operation. Note that the dark circle on the top of the reference area of the glass sample corresponds to a piezo element attached on the backside, which was not operating in this experiment. The SDBD area covered by the discharge is significantly less affected by the icing process or even completely free of ice in the case of the zirconia SDBD which proofs the SDBD anti-icing capability. For additional photos from the iCORE experiment see Supplementary S10.

The FR-4 sample was exposed to a higher air speed, which might be a reason for the ice formation on the SDBD area. The ice accumulated parallel to the electrodes but with a certain distance to them. Supercooled water droplets stick to the 35 µm high electrode and start to form an ice accretion growing towards the flow along the surface. After a significant ice accretion is formed in front of the electrodes, ice in close proximity to the electrode is melted away by the high temperature [23] of the electrode. The result is an ice accretion with a certain distance to the electrodes. In order to support the assumption of

ice accretion initiation on the elevated electrodes, the area of the samples on the side of the high-voltage electrode was examined, see the excerpts on the bottom of Figure 10, which are magnification of the areas marked in green for all samples.

On the area where the discharge is not formed due to the absence of the ground electrode (lighter area) the ice accumulates to the PCB electrodes, but in the case of MEMS samples the ice accretion is distributed homogeneously without specific anchor points. Thus, it can be concluded that MEMS electrodes exhibiting a thickness below 0.3 µm do not provoke the ice attachment in contrast to the 35 µm thick PCB electrodes. Therefore, the advantage of the MEMS fabricated SDBDs for anti-icing applications is well pronounced and can be attributed to the electrode thickness.

The FR-4 SDBD with geometry G2 allows to draw conclusions about a potential influence of the ionic wind. The long electrodes intersect two separate areas of the sample. The upper area of the actuator design generates an ionic wind in downstream direction, while the lower area with symmetrical SDBD design suppresses the ion wind formation. Considering the expansion of the ice free area from the right electrode side one can see that it is independent of the geometry, see Figure 10. Our results improve the confidence of the suggestion made by Meng et al. [23] that the ionic wind does not contribute to the anti-icing effect. Unlike their 70 µm thick electrodes, our MEMS-electrodes provide a direct evidence, as they do not interfere with the flow.

Figure 10 also exhibits that the icing is stronger near the leading edge where the ice accretion is more severe. Whereas on all electrodes of the FR-4 SDBD an ice accretion is visible, only a minor ice accretion is found in the first segment on the glass SDBD, see the slight gray haze in the center excerpt on the bottom of Figure 10. The SDBD area on the zirconia sample is completely free of ice. In aft of the electrodes an ice-free area is formed. We hypothesize that that the heat generated by the discharge is transported downstream and this vortex-induced heat exchange [52] causes the anti-icing effect in the inactive SDBD aft area. Additionally, pre-heated runback water might contribute to the observed anti-icing effect like it is known from conventional heating devices [53].

4.3. De-Icing Results

Subsequently to the anti-icing experiment, the de-icing experiment was performed with the MEMS-SDBDs. For this purpose, the plasma operation was stopped, and the samples were iced for additional 2 min with the same test conditions, see Figure 11.
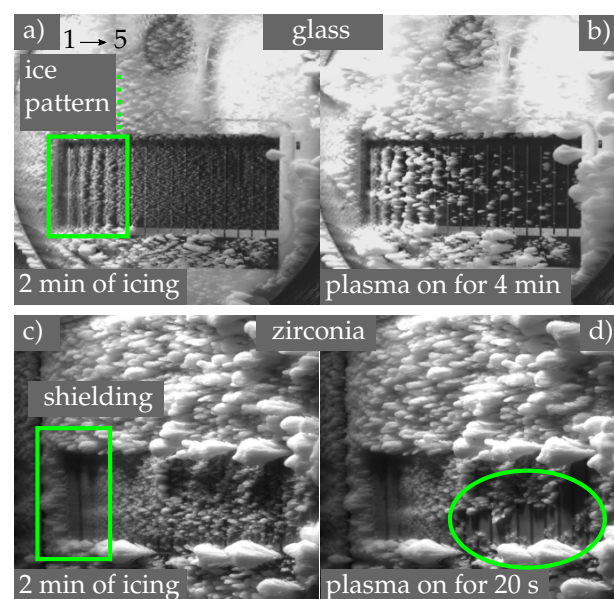

Figure 11. Images taken by the machine vision camera of the de-icing study with the glass and the zirconia SDBD. The SDBDs were turned off for 2 min to ice the former active surface. Pictures (**b**–**d**) present the study after the de-icing time displayed in the lower left corner.

Without discharge the ice started to cover the SDBD area. At the first five electrodes of the glass sample the ice accumulation followed the electrode pattern, see the green mark in Figure 11a. See also Supplementary S11 for the development of the glass SDBD icing. The ice appeared on both sides of the electrodes and the ice structure became less pronounced with an increasing distance from the leading edge. This icing pattern strongly differs from the icing of the FR-4 sample on Figure 10, where the ice was dominantly accumulated at the impact edge of the electrodes along the whole SDBD area. Therefore, the icing pattern of the glass sample is not related to the thickness of the MEMS-electrodes. However, the reason for the icing pattern to be seen is still unclear. Possibly, this effect can be connected to an inhomogeneous cooling of the sample which is less pronounced with the distance from the leading edge due to the residual heat which is transported by the wind in downstream direction. Additionally, it has to be noted that the ice that is accumulated in front of the SDBD area acts as mechanical shield for the ice wind. The shape of the shield is parallel to the electrode structure. The shielding of the ice wind is well visible for zirconia sample, see Figure 11c, where the height of the shield is higher and, thus, the the first zirconia SDBD electrodes depicted a minor icing.

Switching on the plasma after 2 min of icing leads to a recognizable de-icing of both SDBDs. For the glass sample the icing is still strong at the front half of the SDBD because the ice structures are linked to each other. Along the downstream direction of the SDBD, the ice-free area increases gradually. Over all experiments, the initial crack in the glass sample grew and after 4 min of plasma activation during the shown de-icing test the SDBD was damaged which was the cause for aborting the glass sample experiment.

A visible de-icing was evident at the zirconia SDBD 20 s after the plasma activation, which is marked by a green circle in Figure 11d. Similar to the glass SDBD, de-icing was first detected in the right half of the SDBD. On closer inspection, one can see that the ice started to melt near the area that has already been de-iced. After 20 s of plasma activation during the de-icing test of the zirconia sample an electrical breakdown occurred which led to the termination of the experiment.

5. SDBD Efficiency

Previous publications and our results demonstrate a significant anti-icing effect of SDBDs. However, the application prospects of the phenomenon are strongly dependent on the efficiency compared to other technologies. The power consumption of the SDBDs and the parameters used in the current study are compared to the literature data in Table 2. Note that it is important to compare the power normalized to the surface area and only few data is available so far.

Ma et al. [54] conducted electro-thermal anti-icing experiments on a composite aircraft component. A hybrid anti-icing system combining thermoelectric and hydrophobic coatings was investigated by Frotin et al. [55]. Tian et al. [22] reported on an anti-icing system with 1 mm thick ABS-shell SDBDs with 35 µm thick copper electrodes arranged in a stripe and a grid-like geometry. Their operation voltage was 17.8 kV$_{pp}$ (stripes) and 19.1 kV$_{pp}$ (grid) at a frequency of about 11 kHz. They showed that the DBD plasma generated by the two investigated geometries can prevent ice accretion on the leading edge.

The zirconia SDBD ($\epsilon_r = 28.3$) has a similar discharge power consumption compared to the SDBDs of Tian et al. [22], see Table 2. However, the glass and PCB SDBD seems to be more efficient since a visible anti-icing effect was achieved at a much lower power consumption. Partly it can be attributed to the dielectric losses, but probably the zirconia SDBD was operated with too much power.

Table 2. Comparison of the power consumption for different anti-icing technologies. The discharge power is the power consumption obtained from the QV-plots which is only applicable for the SDBDs. The system power includes the power required to generate the high voltage. The last there columns present the parameters of the iCORE. The temperature of the supercooled droplets, ice wind speed and the liquid water content (LWC).

Publication	Technology	Discharge Power [kW/m^2]	System Power [kW/m^2]	Temperature [°C]	Wind Speed [m/s]	LWC [g/m³]
Ma et al. [54]	heating device	−	92	−5	90	2
Frotin et al. [55]	heating device	−	62	−5 & −20	21	0.4
Tian et al. [22]	pulsed-SDBD, grid	8.3	31	−7	90	0.5
Tian et al. [22]	pulsed-SDBD, stripes	7.3	28	−7	90	0.5
current work	glass/PCB SDBD	3.1 ± 0.3	19 ± 1	−17.5 ± 1	27 & 50	3
current work	zirconia SDBD	8.9 ± 1	27 ± 2	−20	30	3

An additional power dissipation required to generate the high-voltage should be accounted for when comparing SDBDs to heating technology. For this purpose, the system power consumption P_{sys} (Chroma output power) was measured before the voltage transformer. Table 2 indicates that our transformer losses are comparable to the one of Tian et al. [22]. The system power consumption of the SDBDs is significantly lower than for the heating devices presented by Ma et al. [54] and Frotin et al. [55].

The total plugin-power measured before the waveform generator for the FR-4 SDBD was 160 W (95 kW m^{-2}). The laboratory power supply is designed for generation of a stable sinusoidal waveform of different frequencies up to 1 kHz, which can be applied to SDBDs of different geometries. Therefore, it is not optimized for a maximum power efficiency at fixed SDBD operation parameters, discharge geometry and load of the discharge. However, the SDBD plugin power density is comparable with the system power density of the heating devices pointing out the high potential of SDBD anti-icing systems.

It can be noted that the electrical power consumed by the plasma for a freely expanding SDBD scales cubic with the applied voltage [43] and quadratic with the dielectric losses [56]. However, when the discharge occupies the whole surface area, the further power increase is linear. The contribution of the dielectric losses to the system power is larger, if the SDBD operates at voltages higher than required for the discharge expansion. Excessive heating of the bulk dielectric alters the working principle of the SDBD to that of an heating device severely limiting the efficiency. The voltage required for the discharge expansion over the whole area depends on the SDBD geometry and the ambient pressure. This observation provides an extra opportunity for the optimization of the SDBD efficiency.

Additionally, we would like to emphasize the observed gradient of icing. Electrodes located further downstream already benefit from a partial deicing of the previous ones. Thus, the SDBD efficiency can be optimized by varying the discharge power density over the aerodynamic component. The highest power density should be at the leading edge and it can be reduced along the wing camber. Two strategies can be applied for the variation of the power density. The first one is to vary the density of the SDBD segments. Technically, this seems to be the simplest solution. However, it must be taken into account that a too small electrode distance would limit the discharge power due to a restriction of the discharge expansion as well as a compensation of the electric field between neighboring electrodes of the same potential. We conjecture that this circumstance can be addressed by a phase-shifted excitation of the electrodes as it was investigated, e.g., by Roth et al. [57] in the context of the ionic wind generation. The second strategy is to vary the dielectric thickness of the SDBD. A smaller dielectric thickness (and larger dielectric constant) provides a stronger increase of the discharge power with the applied voltage, see Figures 7 and 8 as well as the results of Hink et al. [34] and Pipa et al. [43].

6. Summary

MEMS-fabricated SDBDs were investigated for their anti- and de-icing capability. The samples based on the dielectrics borofloat glass and zirconia with PVD-evaporated

Chrome-Nickel and Titanium electrodes were successfully tested in the icing wind tunnel at air speeds between $27 \, \mathrm{m \, s^{-1}}$ and $50 \, \mathrm{m \, s^{-1}}$, and a temperature of $-18 \, °\mathrm{C}$. The air speed was restricted due to an insufficient robustness of the borofloat SDBD against mechanical stress caused by the aerodynamic load.

The performance of the MEMS-manufactured SDBDs has been compared to conventional SDBDs that were realized using printed circuit board (PCB) technology with FR-4 as substrate. The surface roughness of all tested substrates was below $1 \, \mu\mathrm{m}$ and had no discernible impact on the ice accretion. Similarly, the $200 \, \mathrm{nm}$ thick MEMS-electrodes did not act as icing initiators, contrary to the $35 \, \mu\mathrm{m}$ PCB-electrodes. Note that the minimum thickness of PCB electrodes is limited to about $17 \, \mu\mathrm{m}$ for technical feasibility reasons.

This unambiguously indicates an advantage of the MEMS-samples for anti-icing applications due to the unique ability to manufacture sub-micrometer thick electrodes.

It is important to note that the surface wettability plays a crucial role for conceivable anti-icing applications. Hydrophobic substrates demonstrate a better performance when the SDBD is inactive and should therefore be preferred. Smielak et al. [58] showed that the wettability of zirconia can be influenced with the manufacturing process, which could improve further iterations of zirconia SDBDs.

We showed that the anti-icing effect is independent on the ionic wind, which would require a certain minimum thickness of the substrate to avoid the actuator saturation mode. Therefore, the use of thin-film substrates can reduce the ignition voltage.

Worst case estimations clearly prove that the electrical power dissipated in the dielectric does not exceed 30% of the total SDBD-power. A large part of the power is converted by the plasma which extends only a few millimeters above the surface. This fact underscores the potential of low-temperature plasma anti-icing systems in which, unlike thermal systems, the energy is not first converted into heating of the bulk substrate, which then melts the ice in a subsequent process.

We hypothesize that an optimized SDBD tuned to the local icing severity by varying the electrode density and the dielectric thickness will result in a drastic improvement in efficiency.

Abbreviations

The following abbreviations are used in this manuscript:

ABS	Acrylonitrile Butadiene Styrene
EB-PVD	Electron Beam Physical Vapor Deposition
iCORE	Icing and Contamination Research facility
LWC	Liquid Water Content
MEMS	Micro Electro Mechanical Systems
MVD	Median Volumetric Diameter
PCB	Printed Circuit Board
PA	Plasma Actuator
RMS	Root Mean Square
SDBD	Surface Dielectric Barrier Discharge
SEM	Scanning Electron Microscope

References

1. Bragg, M. Effect of geometry on airfoil icing characteristics. *J. Aircr.* **1984**, *21*, 505–511. [CrossRef]
2. Vercillo, V.; Karpen, N.; Laroche, A.; Guillén, J.; Tonnicchia, S.; Andrade Jorge, R.; Bonaccurso, E. Analysis and modelling of icing of air intake protection grids of aircraft engines. *Cold Reg. Sci. Technol.* **2019**, *160*, 265–272. [CrossRef]
3. Thomas, S.; Cassoni, R.; MacArthur, C. Aircraft anti-icing and de-icing techniques and modeling. *J. Aircr.* **1996**, *33*, 841–854. [CrossRef]
4. Drury, M.; Szefi, J.; Palacios, J. Full-scale testing of a centrifugally powered pneumatic de-icing system for helicopter rotor blades. *J. Aircr.* **2017**, 54, 220–228. [CrossRef]
5. Blaha, B.; Evanich, P. *Pneumatic Boot for Helicopter Rotor Deicing*; National Aeronautics: Washington, DC, USA, 1981.
6. Dong, W.; Zhu, J.; Zheng, M.; Chen, Y. Thermal analysis and testing of nonrotating cone with hot-air anti-icing system. *J. Propuls. Power* **2015**, *31*, 896–903. [CrossRef]
7. Al-Khalil, K. Thermo-Mechanical Expulsive Deicing System-TMEDS. In Proceedings of the 45th AIAA Aerospace Sciences Meeting Furthermore, Exhibit, Reno, NV, USA, 8–11 January 2007; p. 692.
8. Vertuccio, L.; De Santis, F.; Pantani, R.; Lafdi, K.; Guadagno, L. Effective de-icing skin using graphene-based flexible heater. *Compos. Part Eng.* **2019**, *162*, 600–610. [CrossRef]
9. Lai, C.; Fu, H.; Hu, B.; Ling, Z.; Jiang, L. Aerodynamic Drag Reduction and Optimization of MIRA Model Based on Plasma Actuator. *Actuators* **2020**, *9*, 64. [CrossRef]
10. Lo, K.; Sriram, R.; Kontis, K. Wake Flow Characteristics over an Articulated Lorry Model with/without AC-DBD Plasma Actuation. *Appl. Sci.* **2019**, *9*, 2426. [CrossRef]
11. Chen, J.; Liang, H.; Wu, Y.; Wei, B.; Zhao, G.; Tian, M.; Xie, L. Experimental Study on Anti-Icing Performance of NS-DBD Plasma Actuator. *Appl. Sci.* **2018**, *8*, 1889. [CrossRef]
12. Yu, J.; Yu, J.; Chen, F.; Wang, C. Numerical study of tip leakage flow control in turbine cascades using the DBD plasma model improved by the parameter identification method. *Aerosp. Sci. Technol.* **2019**, *84*, 856–864. [CrossRef]
13. Abdollahzadeh, M.; Pascoa, J.; Oliveira, P. Comparison of DBD plasma actuators flow control authority in different modes of actuation. *Aerosp. Sci. Technol.* **2018**, *78*, 183–196. [CrossRef]
14. Ebrahimi, A.; Hajipour, M. Flow separation control over an airfoil using dual excitation of DBD plasma actuators. *Aerosp. Sci. Technol.* **2018**, *79*, 658–668. [CrossRef]
15. Kriegseis, J.; Simon, B.; Grundmann, S. Towards in-flight applications? A review on dielectric barrier discharge-based boundary-layer control. *Appl. Mech. Rev.* **2016**, *68*, 020802. [CrossRef]
16. Pescini, E.; De Giorgi, M.; Suma, A.; Francioso, L.; Ficarella, A. Separation control by a microfabricated SDBD plasma actuator for small engine turbine applications: Influence of the excitation waveform. *Aerosp. Sci. Technol.* **2018**, *76*, 442–454. [CrossRef]
17. Sato, S.; Enokido, T.; Ashikawa, K.; Matsubara, M.; Kanie, K.; Ohnishi, N. Development of a flexible dielectric-barrier-discharge plasma actuator fabricated by inkjet printing using silver nanoparticles-based ink. *Sens. Actuators Phys.* **2021**, *2021*, 112823. [CrossRef]
18. Rodrigues, F.; Abdollahzadeh, M.; Pascoa, J.; Oliveira, P. An Experimental Study on Segmented-Encapsulated Electrode Dielectric-Barrier-Discharge Plasma Actuator for Mapping Ice Formation on a Surface: A Conceptual Analysis. *J. Heat Transf.* **2021**, *143*, 011701. [CrossRef]
19. Benmoussa, A.; Páscoa, J. Cycloidal rotor coupled with DBD plasma actuators for performance improvement. *Aerosp. Sci. Technol.* **2021**, *110*, 106468. [CrossRef]
20. Baranov, S.; Chernyshev, S.; Khomich, V.; Kiselev, A.; Kuryachii, A.; Moshkunov, S.; Rebrov, I.; Sboev, D.; Tolkachev, S.; Yamshchikov, V. Experimental cross-flow control in a 3D boundary layer by multi-discharge plasma actuators. *Aerosp. Sci. Technol.* **2021**, *112*, 106643. [CrossRef]
21. Cai, J.; Tian, Y.; Meng, X.; Han, X.; Zhang, D.; Hu, H. An experimental study of icing control using DBD plasma actuator. *Exp. Fluids* **2017**, *58*, 1–8. [CrossRef]

22. Yongqiang, T.; Zhang, Z.; Jinsheng, C.; Leilei, Y.; Lei, K. Experimental study of an anti-icing method over an airfoil based on pulsed dielectric barrier discharge plasma. *Chin. J. Aeronaut.* **2018**, *31*, 1449–1460.

23. Meng, X.; Hu, H.; Li, C.; Abbasi, A.; Cai, J.; Hu, H. Mechanism study of coupled aerodynamic and thermal effects using plasma actuation for anti-icing. *Phys. Fluids* **2019**, *31*, 037103. [CrossRef]

24. Meng, X.; Cai, J.; Tian, Y.; Han, X.; Zhang, D. Experimental Study of Anti-icing and Deicing on a Cylinder by DBD plasma actuation. In Proceedings of the 47th AIAA Plasmadynamics and Lasers Conference, **2016**; p. 4019.

25. Kolbakir, C.; Hu, H.; Liu, Y.; Hu, H. An experimental study on different plasma actuator layouts for aircraft icing mitigation. *Aerosp. Sci. Technol.* **2012**, *107*, 106325. [CrossRef]

26. Chen, Z. A Phenomenon Study on Spreading and Evaporating Process of Droplet on DBD Actuator for Wind Turbine Anti-icing. *IOP Conf. Ser. Earth Environ. Sci.* **2020**, *453*, 012049. [CrossRef]

27. Wei, B.; Wu, Y.; Liang, H.; Zhu, Y.; Chen, J.; Zhao, G.; Song, H.; Jia, M.; Xu, H. SDBD based plasma anti-icing: A stream-wise plasma heat knife configuration and criteria energy analysis. *Int. J. Heat Mass Transf.* **2019**, *138*, 163–172. [CrossRef]

28. Lindner, M.; Berndt, D.; Tschurtschenthaler, K.; Ehrlich, I.; Jungbauer, B.; Schreiner, R.; Pipa, A.; Hink, R.; Foest, R.; Brandenburg, R.; et al. Aircraft Icing Mitigation by DBD-based Micro Plasma Actuators. In *AIAA Aviation 2020 Forum*; AIAA: Reston, VA, USA, 2020; p. 3243.

29. Gao, T.; Luo, Z.; Zhou, Y.; Yang, S. A novel de-icing strategy combining electric-heating with plasma synthetic jet actuator. *Proc. Inst. Mech. Eng. Part J. Aerosp. Eng.* **2021**, *235*, 513–522. [CrossRef]

30. Niu, J.; Sang, W.; Zhou, F.; Li, D. Numerical investigation of an anti-icing method on airfoil based on the NSDBD plasma actuator. *Aircr. Eng. Aerosp. Technol.* **2021**, *93*. [CrossRef]

31. Rodrigues, F.; Pascoa, J.; Trancossi, M. Heat generation mechanisms of DBD plasma actuators. *Exp. Therm. Fluid Sci.* **2018**, *90*, 55–65. [CrossRef]

32. Lindner, M.; Berndt, D.; Ehrlich, I.; Jungbauer, B.; Schreiner, R.; Pipa, A.; Hink, R.; Foest, R.; Brandenburg, R.; Max, A.; et al. Fabrication, surface integration and testing of miniaturized dielectric barrier discharge plasma actuators for active flow control applications. In *AIAA Aviation 2019 Forum*; AIAA: Reston, VA, USA, 2019; p. 2998.

33. Houser, N.; Gimeno, L.; Hanson, R.; Goldhawk, T.; Simpson, T.; Lavoie, P. Microfabrication of dielectric barrier discharge plasma actuators for flow control. *Sens. Actuators Phys.* **2013**, *201*, 101–104. [CrossRef]

34. Hink, R.; Pipa, A.; Schaefer, J.; Caspari, R.; Weichwald, R.; Foest, R.; Brandenburg, R. Influence of dielectric thickness and electrode structure on the ion wind generation by micro fabricated plasma actuators. *J. Phys. Appl. Phys.* **2020**, *53*, 405201. [CrossRef]

35. Okochi, S.; Kasagi, N.; Suzuki, Y.; Ito, S. Development of micro plasma actuator for active flow control. In Proceedings of the 7th World Conference On Experimental Heat Transfer, Fluid Mechanics, Furthermore, Thermodynamics, Krakow, Poland, 28 June–3 July 2009.

36. Durscher, R.; Roy, S. Three-dimensional flow measurements induced from serpentine plasma actuators in quiescent air. *J. Phys. Appl. Phys.* **2012**, *45*, 035202. [CrossRef]

37. Pescini, E.; De Giorgi, M.; Francioso, L.; Taurino, A.; Martucci, M.; Lavoie, P. Electrode material degradation monitoring for durable dielectric barrier discharge plasma actuators manufacturing. In Proceedings of the 54th AIAA Aerospace Sciences Meeting, **2016**; p. 0196.

38. Pons, J.; Oukacine, L.; Moreau, E.; Tatibouet, J. Observation of dielectric degradation after surface dielectric barrier discharge operation in air at atmospheric pressure. *IEEE Trans. Plasma Sci.* **2008**, *36*, 1342–1343. [CrossRef]

39. Berndt, D.; Lindner, M.; Schreiner, R.; Hink, R.; Pipa, A.; Schaefer, J.; Brandenburg, R.; Foest, R.; Geils, J.; Sander, A.; Others Realization of Multifunctional Surfaces Containing MEMS-based DBD Plasma Actuators and Biomimetic Structures for Flow Manipulation. In *AIAA Aviation 2019 Forum*; AIAA: Reston, VA, USA, 2019; p. 2999.

40. Pipa, A.; Brandenburg, R. The equivalent circuit approach for the electrical diagnostics of dielectric barrier discharges: The classical theory and recent developments. *Atoms* **2019**, *7*, 14. [CrossRef]

41. Manley, T. The electric characteristics of the ozonator discharge. *Trans. Electrochem. Soc.* **1943**, *84*, 83. [CrossRef]

42. Piferi, C.; Barni, R.; Roman, H.; Riccardi, C. Current Filaments in Asymmetric Surface Dielectric Barrier Discharge. *Appl. Sci.* **2021**, *11*, 2079. [CrossRef]

43. Pipa, A.; Hink, R.; Foest, R.; Brandenburg, R. Dependence of dissipated power on applied voltage for surface barrier discharge from simplest equivalent circuit. *Plasma Sources Sci. Technol.* **2020**, *29*, 12LT01. [CrossRef]

44. Scherrer, B.; Schlupp, M.; Stender, D.; Martynczuk, J.; Grolig, J.; Ma, H.; Kocher, P.; Lippert, T.; Prestat, M.; Gauckler, L. On proton conductivity in porous and dense yttria stabilized zirconia at low temperature. *Adv. Funct. Mater.* **2013**, *23*, 1957–1964. [CrossRef]

45. Schott Schott Borofloat33. 2021. Available online: https://www.metaglas.de/fileadmin/dokumente/pdf/LGS-Borofloat.pdf (accessed on 19 October 2021).

46. WE Datenblatt Standard FR4 TG135. 2021. Available online: https://www.wedirekt.de/.../FR4TG135_DE.pdf (accessed on 19 October 2021).

47. Hauk, T.; Strobl, T.; Raps, D. Implementation and calibration of the icing and contamination research facility (iCORE). In Proceedings of the ILASS-Europe, 25th European Conference on Liquid Atomization Furthermore Spray Systems, Chania, Greece, 1–4 September 2013; Volume 1.

48. Vercillo, V. Durable Laser Patterned Metal Surfaces with Enhanced Icephobic Properties for Aerospace Applications. Ph.D. Thesis, Technische Universität Dresden, Dresden, Germany, 2020.

49. Makkonen, L. Models for the growth of rime, glaze, icicles and wet snow on structures. *Philos. Trans. R. Soc. London. Ser. Math. Phys. Eng. Sci.* **2000**, *358*, 2913–2939. [CrossRef]

50. Momen, G.; Jafari, R.; Farzaneh, M. Ice repellency behaviour of superhydrophobic surfaces: Effects of atmospheric icing conditions and surface roughness. *Appl. Surf. Sci.* **2015**, *349*, 211–218. [CrossRef]

51. Roisman, I.; Rioboo, R.; Tropea, C. Normal impact of a liquid drop on a dry surface: Model for spreading and receding. *Proc. R. Soc. London. Ser. Math. Phys. Eng. Sci.* **2002**, *458*, 1411–1430. [CrossRef]

52. Jacobi, A.; Shah, R. Heat transfer surface enhancement through the use of longitudinal vortices: A review of recent progress. *Exp. Therm. Fluid Sci.* **1995**, *11*, 295–309. [CrossRef]

53. Zheng, M.; Dong, W.; Guo, Z.; Lei, G. Analysis of Runback Water Flow on Anti-Icing Surface Using Volume-of-Fluid Method. In Proceedings of the Turbo Expo: Power for Land, Sea, and Air, Charlotte, NC, USA, 26 June 2017,; p. 50879.

54. Hui, M.; Dalin, Z.; Fanxin, M. Others Experiment of Electro-thermal Anti-icing on a Composite Assembly. *Acta Aeronaut. Astronaut. Sin.* **2013**, *34*, 8.

55. Fortin, G.; Adomou, M.; Perron, J. *Experimental Study of Hybrid Anti-Icing Systems Combining Thermoelectric and Hydrophobic Coatings*; SAE Technical Paper; SAE: Warrendale, PA, USA, 2011,

56. Küchler, A. *Hochspannungstechnik*; Springer: Berlin/Heidelberg, Germany, 2009.

57. Roth, J.; Sin, H.; Madhan, R.; Wilkinson, S. Flow re-attachment and acceleration by paraelectric and peristaltic electrohydrodynamic (EHD) effects. In Proceedings of the 41st Aerospace Sciences Meeting Furthermore, Exhibit, Reno, NV, USA, 6–9 January 2003; p. 531.

58. Smielak, B.; Klimek, L.; Wojciechowski, R.; Bąkała, M. Effect of zirconia surface treatment on its wettability by liquid ceramics. *J. Prosthet. Dent.* **2019**, *122*, e1–e6. [CrossRef]